Cosmological Fisher forecasts for next-generation spectroscopic surveys

William d'Assignies D., Cheng Zhao, Jiaxi Yu, Jean-Paul Kneib

Monthly Notices of the ROYAL ASTRONOMICAL SOCIETY

MNRAS **521,** 3648–3662 (2023) https://doi.org/10.1093/mnras/stad611
Advance Access publication 2023 March 23

Cosmological Fisher forecasts for next-generation spectroscopic surveys

William d'Assignies D. [1,2,3]★ Cheng Zhao [1]★ Jiaxi Yu[1] and Jean-Paul Kneib[1,4]

[1]*Laboratory of Astrophysics, École Polytechnique Fédérale de Lausanne (EPFL), Observatoire de Sauverny, CH-1290 Versoix, Switzerland*
[2]*Institut de Física d'Altes Energies (IFAE), The Barcelona Institute of Science and Technology, Campus UAB, E-08193 Bellaterra (Barcelona) Spain*
[3]*Physics institute of the École Normale Supérieure PSL, 24 rue Lhomond, F-75005 Paris, France*
[4]*Aix Marseille Université, CNRS, LAM (Laboratoire d'Astrophysique de Marseille) UMR 7326, F-13388 Marseille, France*

Accepted 2023 February 23. Received 2023 February 23; in original form 2023 January 10

ABSTRACT

Next-generation spectroscopic surveys such as the MegaMapper, MUltiplexed Survey Telescope (MUST), MaunaKea Spectroscopic Explorer (MSE), and WideField Spectroscopic Telescope (WST) are foreseen to increase the number of galaxy/quasar redshifts by an order of magnitude, with hundred millions of spectra that will be measured at $z > 2$. We perform a Fisher matrix analysis for these surveys on the baryonic acoustic oscillation (BAO), the redshift-space distortion (RSD) measurement, the non-Gaussianity (NG) amplitude $f_{\rm NL}$, and the total neutrino mass M_ν. For BAO and RSD parameters, these surveys may achieve precision at sub-per cent level (<0.5 per cent), representing an improvement of factor 10 w.r.t. the latest data base. For NG, these surveys may reach an accuracy of $\sigma(f_{\rm NL}) \sim 1$. They can also put a tight constraint on M_ν with $\sigma(M_\nu) \sim 0.02$ eV if we do joint analysis with Planck and even 0.01 eV if combined with other data. In addition, we introduce a general survey model to derive the cosmic volume and number density of tracers, given instrumental facilities and survey strategy. Using our Fisher formalism, we can explore (continuously) a wide range of survey observational parameters and propose different survey strategies that optimize the cosmological constraints. Fixing the fibre number and survey duration, we show that the best strategy for $f_{\rm NL}$ and M_ν measurement is to observe large volumes, despite the noise increase. However, the strategy differs for the apparent magnitude limit. Finally, we prove that increasing the fibre number improves M_ν measurement but not significantly $f_{\rm NL}$.

Key words: neutrinos – techniques: spectroscopic – surveys – cosmological parameters – early Universe – large-scale structure of Universe.

1 INTRODUCTION

Massive high-redshift spectroscopic survey aims at exploring baryon acoustic oscillations (BAO) and the growth of structure through redshift-space distortions (RSDs) with large-scale structures (LSS) in the Universe, by probing the 3D distribution of galaxies and quasars in a wide area. LSS also provides one of our best windows on fundamental physics, such as properties of the early Universe with the non-Gaussian primordial fluctuations, or the sum of neutrino mass (NM). As the product of spectroscopic surveys, the data base for the 3D positions of galaxies and quasars has been growing rapidly. In the past decade, surveys like the SDSS-III Baryon Oscillation Spectroscopic Survey (BOSS; Schlegel, White & Eisenstein 2009) and SDSS-IV extended BOSS (eBOSS; Dawson et al. 2016) have measured millions of spectra. The ongoing Dark Energy Survey Instrument (DESI; DESI Collaboration et al. 2016) is expected to take over 30 million spectra in 5 yr. The next-generation experiments, such as the MegaMapper (Schlegel, Kollmeier & Ferraro 2019), MUltiplexed Survey Telescope[1] (MUST), WideField Spectroscopic Telescope (WST; Ellis & Dawson 2019), and the MaunaKea Spectroscopic Explorer (MSE; Percival et al. 2019), are expected to be equipped with a large number of fibres (10–20 k) thanks to the development of robotic fibre positioners and are foreseen to increase the number of observed galaxy/quasar by another order of magnitude.

These observations will allow us to test the standard ΛCDM model of cosmology, with parameters constrained at sub-per cent-level precision. The standard ΛCDM model has been able to explain a large number of observations, from the cosmic microwave background (CMB) to low-redshift galaxies. However, tensions between measurements have recently become more and more significant, notably the Hubble constant H_0 (Riess et al. 2019; Freedman 2021) and the growth parameter σ_8 (Macaulay, Wehus & Eriksen 2013; Douspis, Salvati & Aghanim 2019). The origin of these tensions could come from bias in our measurements, unknown systematics, or be the sign of new physics (Vagnozzi 2020; Di Valentino et al. 2021; Nunes & Vagnozzi 2021; Blanchard et al. 2022). There are extensions of the standard ΛCDM model, e.g. varying the dark energy equation of state (Copeland, Sami & Tsujikawa 2006; Tripathi, Sangwan & Jassal 2017), the primordial non-Gaussianity (NG; Matarrese, Verde & Jimenez 2000; Dalal et al. 2008), and the non-zero total NM (Boyle 2019).

The primordial non-Gaussianity is a test to inflation scenario (Achúcarro et al. 2022), and the LSS of galaxies/quasars is controlled by the NG amplitude parameter $f_{\rm NL}$ through a bias scale dependence (Maldacena 2003; Desjacques, Seljak & Iliev 2009). Therefore, measuring the large-scale clustering of galaxies provides an opportunity to study the early Universe physics.

Oscillation experiments have shown that at least two families of neutrinos have non-zero mass (Capozzi et al. 2016), but they can only

★ E-mail: wdoumerg@ifae.es (WdD); cheng.zhao@epfl.ch (CZ)
[1]https://must.astro.tsinghua.edu.cn

constrain the relative mass difference between families. Normal and inverted hierarchy theories give different predictions of the minimal sum of NM, respectively: $M_\nu \sim 0.06$ eV, or $M_\nu \sim 0.1$ eV (Qian & Vogel 2015). As massive neutrinos constitute a small fraction of the energy density of the Universe, a range of cosmological probes can provide indirect evidence of their mass properties (Lesgourgues & Pastor 2014). For example, a joint analysis of the Planck CMB measurements and the Baryon Oscillation Spectroscopic Survey (BOSS) galaxy clustering data have already put an upper limit $M_\nu < 0.16$ eV at 95 per cent confidence level (Ivanov, Simonović & Zaldarriaga 2020) and down to $M_\nu < 0.11$ eV with data from eBOSS (Alam et al. 2021). Thus, the Universe appears to be an ideal laboratory for the measurement of the neutrino hierarchy. However, it has been recently objected that this measurement depends on the ΛCDM model (which has started to exhibit weakness) and cannot categorically exclude a scenario, though a careful study on the dependence of these constraints on the ΛCDM model may be necessary (Boyle & Komatsu 2018).

The aim of this article is first to forecast the accuracy of high-redshift spectroscopic surveys of the next decade on four cosmological aspects: BAO scales, the RSD effect, NG amplitude parameters, and the sum of NM. We use Fisher information matrix *F*ij (Tegmark 1997) for this purpose, assuming its inverse is a typical covariance matrix of our parameters (which is true in the Gaussian case and gives an upper limit in the general one). We will use the linear theory to evaluate this information matrix. Thus, our forecasting method is not particularly innovative compared to modern Markov chain Monte Carlo (MCMC; Chudaykin & Ivanov 2019) methods, and the consideration of non-linearity. Our goal is rather to compare the different surveys and to apply this simple formalism in the context of an optimization of the parameters of a survey. In principle, it is also possible to perform Fisher forecasts for surveys probing $z \sim 1$, with a much higher tracer density. None the less, the main interest of these surveys is to extract more information from small scales, e.g. by exploring the power spectrum up to $k_{\rm max} \sim 0.5h$ Mpc^{-1} modes. The linear model of the power spectrum that we adopt in this study is not able to describe these scales accurately. Therefore, forecasts for high-density surveys that focus on small-scale clustering are left for future work.

With the increase of the number of fibre, and as demonstrated by our forecasts, future surveys will be able to constrain cosmological parameters such as BAO and RSD at the sub-per cent level. Besides, the measurement of parameters beyond the standard model like $f_{\rm NL}$ and M_ν remains a challenge as the error bars are comparable to the parameter values. That is why, in a second step, we produce a quantitative optimization pipeline of the observation strategy of spectroscopic surveys for the study of the parameters $f_{\rm NL}$ and M_ν as we find their constraints still need improvement despite their large number of fibres and large cosmic volume. It could be used for the design of future surveys, but it also provides a point of comparison between the expected accuracy of some surveys and the technically optimal one. To do so, we will present a rather general model of a high-redshift spectroscopic survey. We model in a simplified way the properties of observational targets, the specifications of the telescope, and the survey strategy.

This paper is organized as follows. In Section 2, we describe the future high-redshift massive spectroscopic surveys in detail. The methodology used for the science forecasts is outlined in Section 3, as well as our modelling for a general spectroscopic survey. We present the cosmological parameter constraints and the preferred improvements for future surveys in Section 4. Finally, we summarize our results in Section 5.

2 SURVEYS

In this section, we describe various spectroscopic galaxy surveys and cosmological probes considered in our forecasts. These surveys will observe emission line galaxies (ELGs) that are abundant up to redshift ∼2 (Madau & Dickinson 2014), Lyman alpha emitter galaxies (LAEs), Lyman break galaxies (LBGs), and BX galaxies (Steidel et al. 2004) that can be observed up to redshift 5, or even higher in theory (Wilson & White 2019). Forecasts presented in this work do not include constraints on cosmological parameters coming from cosmic shear, HI intensity mapping, and future CMB observations that will be included in upcoming surveys (Annis, Newman & Slosar 2022) such as Euclid (Laureijs et al. 2011), DESI (DESI Collaboration et al. 2016), Puma (Slosar et al. 2019), and HETDEX (Adams et al. 2011).

Survey properties considered in our study are listed in Table 1, and the associated densities are presented in Section 4. In general, the number density of a given tracer *X* can be (ideally) modelled by

$$n(z) = \int^{m_{\rm max}} E(m)\phi_X(m, z)dm, \tag{1}$$

where m is the apparent magnitude of the tracer, $m_{\rm max}$ is the maximum apparent magnitude of the survey, $E(m)$ is the efficiency of observation, and ϕ_X is the tracer luminosity function. If the efficiency is independent of the magnitude, it reduces to

$$n(z) = {\rm e_{ff}} \cdot n_X(m_{{\rm max},z}), \tag{2}$$

where $\rm e_{ff}$ is the constant efficiency of the tracer, and n_X is the theoretical tracer density (cf. Section 3.2). We consider a redshift uncertainty $\sigma_z/(1+z) = 0.001$ (Percival et al. 2019) for every survey. Indeed, the redshift resolution is assumed to be similar but slightly more conservative than DESI one (DESI Collaboration et al. 2016) to ensure that it is a reasonable estimation across our wavelength range.

2.1 MegaMapper

MegaMapper (Schlegel et al. 2019) is a spectroscopic instrument that will be located at the Las Campanas observatory in the southern hemisphere. It would target LBG at high redshift $2 < z < 5$, covering 14 000 deg^2 of the sky. Its 6.5-m telescope, 20 000 fibres, and a 5-yr observation period would yield a galaxy number density $n > 10^{-4}h^3$Mpc^{-3} across its redshift range. For the property of the fiducial LBG sample, we use the values in Table 2 of Ferraro & Wilson (2019). These values are compatible with the model given by equation (2), with $n_{\rm LBG}$ an idealized density distribution introduced in sub-Section 3.2 [equation (9)], $e_{\rm ff} = 0.4$ for $z < 4$, $e_{\rm ff} = 0.9$ for $4 < z < 5$ (see fig. 4 of Sailer et al. 2021), and $m_{\rm max} = 24.5$.

2.2 MSE

The MaunaKea Spectroscopic Explorer (MSE; Percival et al. 2019) will be located in Hawaii in the Northern hemisphere, probing over 10 000 deg^2. It will couple an 11.25-m mirror with a 1.5-deg^2 field of view (FoV) to 4000 fibres, feeding to spectrographs that cover 360–1300 nm. This design enables the detection of ELGs at $1.6 < z < 2.4$ and LBGs at $2.4 < z < 4$. The exposure time is 1800 s. The ELG number density shown in Table 4 is taken from Percival et al. (2019). For LBG, we will assume a model described by equation (1). We estimate the efficiency thanks to fig. 2 of Percival et al. (2019), assuming that 40 per cent of LBG have Equivalent Width values EW < 0, 30 per cent have $0 <$ EW < 20 and 30 per cent have EW $>$

Table 1. Properties of future surveys, including their tracers, the redshift range and sky coverage, the number of fibres, the telescope diameter, and the telescope location. Most of these properties are not definitive yet.

Survey	Tracer	Redshift Range	Sky coverage (deg^2)	Fibre Number	Telescope size (m)	Location
MegaMapper	LBG	$2 < z < 5$	14 000	20 000	6.5	Las Campanas Observatory Chile
MSE	ELG	$1.6 < z < 2.4$	10 000	4332	11.25	Mauna Kea Observatories Hawaii, USA
	LBG	$2.4 < z < 4$				
WST (or Spectel)	LBG	$2 < z < 5$	15 000	20 000 –60 000	11.4	Northern Chile
MUST	LBG + BX	$2 < z < 4$	9000	10 000	6.5	Lenghu, Qinghai province China
	–LBG+BX + LAE		–15 000	–20 000		

20, and averaging over EW[2]. The effective efficiency law is then given by $E(m) = -0.18m + 4.8$. Given the approximate efficiency rate of 0.5, and the required observed density ($n = 10^{-4}h^3/\mathrm{Mpc}^3$), 1400 fibres/$deg^2$ will be allocated to LBG observations, restricting to a maximum magnitude $m_{\mathrm{max}} = 24.2$ (Percival et al. 2019). We introduced our LBG luminosity function model in sub-Section 3.2.

2.3 MUST

The MUltiplexed Survey Telescope[3] (MUST) is a future 6.5-m telescope (with a 7 deg^2 FoV) located in China in the Northern hemisphere. Its target can be either LBG + BX (LBGX) or a combination of LBGX + LAE. Since the exact survey design is still in flux, our forecast supposes its redshift range to be $2 < z < 4$, with a sky coverage between 9000 and 15 000 deg^2, and fibre numbers to be either 10 000 or 20 000.

2.4 A WST-like NTL survey

The WideField Spectroscopic Telescope[4] (WST; Ellis & Dawson 2019) is a proposed spectroscopic survey in the southern hemisphere that would couple an 11.4-m dish (with a 5-deg^2 FoV) and 20 000–60 000 fibres, enabling more than a hundred million of fibre exposures (each ≥4000-s long) over its survey period. Its design would permit observations of LBGs and LAEs up to redshift 5, with number densities 2–5 times of those for a MegaMapper-like survey. Since the exact design of this survey is a work in progress, we also explore several possible survey parameters.

For the forecast, we consider a similar survey to MegaMapper, with a sky coverage of 15 000 deg^2 for LBG at redshift 2–5, and each tracer can be observed for a period as long as needed until it reaches the required spectrum quality. We model it with an efficiency $e_{\mathrm{ff}} = 0.9$ relative to the theoretical tracer density [cf. equation (2)] but with different maximum magnitudes – 24.2, 24.5, and 25 – depending on the final fibre number. This might correspond to 20,000–40,000–100,000 fibres for 5 yr of observation[5] This forecast somehow represents a cosmological limit on the achievable parameters accuracy, since we are assuming an efficiency very close to 1. As we do not really take into account the final properties of WST in our modelling, we will refer to this fiducial survey as a NTL survey (a No-Time-Limit survey) in Section 4.

2.5 A general survey

We also consider a high-redshift ($z > 2$) general spectroscopic survey with a modelling of the survey settings, in order to explore the optimal strategy that yields the tightest constraints of chosen cosmological parameters. In a first step, we assume an LBG survey lasting 5 yr, based on a 10-m telescope equipped with 20 000 fibres. Since LBGs are abundant mostly at $z \gtrsim 2$ (Wilson & White 2019), we consider a redshift window $[z_{\mathrm{min}}, z_{\mathrm{max}}]$ that always starts with $z_{\mathrm{min}} = 2$. The survey volume will be thus described by the fraction of the survey sky coverage f_{sky}.[6] and the redshift span $\Delta z = z_{\mathrm{max}} - z_{\mathrm{min}}$. In a second step, we will also vary the 'observation capacity' defined as the product of the survey duration and the fibre number to extend this model to a larger variety of spectroscopic telescopes and to highlight the improvement of the measurements with the available technology. We detailed the modelling of such a survey in Section 3.5.

3 METHODOLOGY

In this section, we first describe some properties of observed galaxies. Then, we introduce the commonly used Fisher matrix forecasting technique. In Section 3.4, we specify the BAO, RSD, non-Gaussianity, and NM forecast strategies. We then introduce our modelling of a general survey in Section 3.5.

3.1 Observed power spectrum

The power spectrum of a dark matter tracer X is related to the theoretical matter power spectrum $P_{\mathrm{m}}(k, z)$ with

$$P_X(k, \mu, z) = (b_X(z) + f(z)\mu^2)^2 P_{\mathrm{m}}(k, z), \tag{3}$$

with b_X being the tracer bias, f being the growth rate, and μ being the cosine between the line of sight and the 3D mode $\boldsymbol{k}$. To take into account the error in the redshift measurement $\sigma_z/(1+z)$ that propagates to an error in the radial distance via $\sigma_\chi = \sigma_z c/H(z)$, we multiply the power spectrum by a factor $\exp(-k^2\mu^2\sigma_\chi^2)$ (Sailer et al. 2021).

We also introduce the cross-power spectrum of two different tracers A and B following McDonald & Seljak (2009) as

$$P_{\mathrm{AB}}(k, \mu, z) = (b_{\mathrm{A}}(z) + f(z)\mu^2)(b_{\mathrm{B}}(z) + f(z)\mu^2)P_{\mathrm{m}}(k, z), \tag{4}$$

[2]We are averaging over the three templates $E(m) = 0.4E(m|\mathrm{EW} < 0) + 0.3E(m|0 < \mathrm{EW} < 20) + 0.3E(m|20 < \mathrm{EW})$.
[3]https://must.astro.tsinghua.edu.cn
[4]Previously named Spectel, https://www.wstelescope.com/
[5]Of course, we do not expect surveys to have 100 000 fibres in the next decay. This forecast rather serves as an upper limit.
[6]$f_{\mathrm{sky}} = 1$ corresponds to the full sky, 41 253 deg^2.

Table 2. Fiducial values of cosmological parameters and their Planck Gaussian prior. NG amplitude $f_{\rm NL}$ is neglected except for the NG forecast.

h	$\omega_{\rm b}$	$\omega_{\rm c}$	$n_{\rm s}$	τ	$\ln(A_{\rm s})$	M_ν (eV)
Fiducial values						
0.677	0.02247	0.1192	0.9675	0.056	−13.073	0.06
Planck half-width Gaussian prior						
0.0054	0.00015	0.0012	0.0042	0.007	0.015	0.5

where $b_{\rm A}$ and $b_{\rm B}$ are biases of tracers A and B, respectively. We report in Table 2 fiducial values of six standard cosmological parameters used in this work, along with the extension model parameter M_ν.

Power spectrum will be evaluated using CAMB[7] (Howlett et al. 2012) and PYCCL[8] (Chisari et al. 2019).

3.2 Bias and luminosity function

For ELG, we assume a constant clustering amplitude, based on the analysis of DESI-selected samples in the DEEP2 data (DESI Collaboration et al. 2016). In that case, the bias can be approximated as $b_{\rm ELG} = 0.8 \times D(0)/D(z)$ with D the growth function. Factor 0.8 is chosen to be slightly lower than that of DESI (0.84; see DESI Collaboration et al. 2016) and eBOSS (1; see Dawson et al. 2016), as we consider fainter ELGs in this study.

We model LBG and LAE bias following the parametrization of Wilson & White (2019) using

$$b_{\rm LBG/LAE}(z, m) = A(m)(1+z) + B(m)(1+z)^2, \tag{5}$$

with $A(m) = -0.98(m - 25) + 0.11$ and $B(m) = 0.12(m - 25) + 0.17$, m being the apparent magnitude. We assume that fainter galaxies contribute more, since the galaxy abundance grows as the magnitude increases, and reduce the bias to a one-parameter function $b(z, m) \approx b(z, m_{\rm max})$. For samples with a large magnitude band, we might separate it into sub-samples of different maximal magnitudes and adopt a multitracer approach.

For the aim of our study, we need to evaluate the LBG density function. An idealized number density is modelled by

$$n_{\rm LBG} = \int_{-\infty}^{M_c} \phi(M) dM, \tag{6}$$

with ϕ the luminosity function (Wilson & White 2019; Sailer et al. 2021), and M the absolute magnitude. We use the Schechter model (Schechter 1976) for the luminosity function:

$$\phi(M) = \frac{\ln 10}{2.5}\phi^\star 10^{-0.4(1+\alpha)(M-M^\star)} \exp\left(-10^{-0.4(M-M^\star)}\right) \tag{7}$$

with α, $M^\star$, and $\phi^\star$ listed in table 3 of Wilson & White (2019). The absolute magnitude cutoff $M_{\rm c}$ of galaxies at redshift z with apparent magnitude being $m_{\rm max}$ is determined as

$$M_c(m_{\rm max}) = m_{\rm max} - 5\log_{10}\left(\frac{D_{\rm L}(z)}{10{\rm pc}}\right) + 2.5\log_{10}(1+z), \tag{8}$$

with $D_{\rm L}(z)$ the luminosity distance. As the observation depends rather on the apparent magnitude m than the absolute magnitude M, we rewrite, the density equation, with $\phi(m, z) = \phi(M(m, z))$, using $dM/dm = 1$, as

$$n_{\rm LBG}(z) = \int^{m_{\rm max}} \phi(m, z) dm. \tag{9}$$

[7] https://camb.readthedocs.io/en/latest/
[8] https://ccl.readthedocs.io/en/latest/

In the rest of the study, we will use this last equation formalism and refer to m as 'magnitude' hereafter.

3.3 Fisher matrix

For a set of cosmological parameters $\{p_i\}$, the diagonal coefficient of the inverse of its Fisher matrix $\mathcal{F}_{ij}$ gives an upper bound on the variance of each parameter: $\sigma_i^2 \geq (\mathcal{F})_{ii}^{-1}$ according to the Cramer–Rao inequality (with equality for Gaussian likelihood). We follow the same steps as Zhao et al. (2016) and considered the Fisher matrix

$$\mathcal{F}_{ij} = \frac{V_{\rm sur}}{4\pi^2}\int_{-1}^{+1} d\mu \int_{k_{\rm min}}^{k_{\rm max}} k^2 dk F_{ij}(k, \mu), \tag{10}$$

$$F_{ij} = \frac{1}{2}{\rm Tr}(\partial_{p_i}\mathbf{C}\mathbf{C}^{-1}\partial_{p_j}\mathbf{C}\mathbf{C}^{-1}), \tag{11}$$

with $V_{\rm sur}$ the comoving volume of the survey, and $\mathbf{C}$ the data covariance matrix. The integration bound $k_{\rm min}$ depends on the survey volume and corresponds to the maximal length, while $k_{\rm max}$ depends on the accuracy of the theoretical model on non-linear scales and on the shot noise. We take by default

$$k_{\rm min} = \frac{2\pi}{V_{\rm sur}^{1/3}}[h\,{\rm Mpc}^{-1}],\ k_{\rm max} = \frac{0.1D(0)}{D(z)}[h\,{\rm Mpc}^{-1}]. \tag{12}$$

Since the NM, and more generally many new physics properties, such as the nature of gravity, are significantly encoded at small scales, we will also consider an 'optimistic' integration bound with $k_{\rm max} = 0.3h{\rm Mpc}^{-1}$. This is motivated by both the reduction of shot noise in future data survey and expected progress in theoretical understanding and modelling of non-linearities.

3.3.1 One tracer

When targets are the same type of tracer (MegaMapper LBGs for example), C is a 1×1 matrix. We take into account the tracer distribution discreetness by adding a Poissonian shot noise that scales as the inverse of the number density $1/n$ as

$$C = P + 1/n, \tag{13}$$

where P is the power spectrum of this tracer. Thus, the Fisher matrix is

$$F_{ij} = \frac{1}{2}\left(\frac{nP}{nP+1}\right)^2 \frac{\partial \ln P}{\partial p_i}\frac{\partial \ln P}{\partial p_j}. \tag{14}$$

We will report the parameter $nP(k = 0.14, \mu = 0.6)$ for different surveys, an approximate centre-of-weight point for BAO measurements, to give a qualitative description of the noise level, following DESI Collaboration et al. (2016).

3.3.2 Two tracers

For two tracers (LBG + LAE in MUST for example), C is now a 2×2 matrix, and under the same assumption,

$$\mathbf{C} = \begin{bmatrix} P_{\rm AA} + \frac{1}{n_{\rm A}} & P_{\rm AB} \\ P_{\rm AB} & P_{\rm BB} + \frac{1}{n_{\rm B}} \end{bmatrix}, \tag{15}$$

where $P_{\rm AA}$ and $P_{\rm BB}$ are auto-power spectra of tracers A and B, and $P_{\rm AB}$ is the cross-power spectrum of tracers A and B. An explicit expression for the Fisher matrix in the two tracers case is given in appendix A of Zhao et al. (2016) as combinations of $\frac{\partial \ln P_T}{\partial p_i}$ with $T =$ A, B, AB. In the case of two independent tracers, $\mathbf{C}$ is diagonal and

the two-tracers Fisher matrix is equal to the sum of the two one-tracer matrix. Similarly, as in the one-tracer case, we will report the parameter $\sum n_i P(k = 0.14, \mu = 0.6)$.

For surveys with extremely massive data sets, whose galaxy apparent magnitudes are spread over a wide band, we separate them into sub-samples with different magnitude ranges (typically $\{-\infty; 24.5\}, \{24.5; 24.8\}$). Then, we adopt a two-tracer forecast approach. Such a process is mainly motivated by the non-Gaussianity forecast, since $\delta b \propto f_{\rm NL} b_G$ (cf. Section 3.4.3). Indeed, the bias decreased with the magnitude, and a one-tracer approach with $b = b(m_{\rm max})$ assumption artificially reduces the sensitivity to NG.

3.3.3 Complementary data sets

To combine constraints from two independent surveys[9] A and B that aim to measure the same set of cosmological parameters, one simply adds their Fisher matrix $F_{ij} = F^A_{ij} + F^B_{ij}$. Furthermore, to introduce priors from complementary data sets (such as Planck CMB) that have measured parameters $\{p_i\}$ with accuracies $\{\sigma_i\}$, one simply adds to the Fisher matrix $P_{ij} = \delta_{ij}/\sigma_i^2$ (assuming Gaussian uncertainties).

3.3.4 Redshift bins

Forecasts for a survey that covers a large redshift range $[z_{\rm min}, z_{\rm max}]$ have to take into account the redshift dependence of parameters. There are three approaches to do so:

(i) Split the survey volume into redshift bins $\{z_k\}$ with separation dz_k and present the forecast for each bin separately.
(ii) Separate the survey volume into redshift bins $\{z_k\}$ with separation dz_k, and sum the Fisher matrices, neglecting cross-correlation between bins: $F_{ij} = \sum_k F^{z_k}_{ij}$.
(iii) Consider one redshift bin, with an effective redshift $z_{\rm eff}$ (so with this approach, one neglects redshift dependence of the parameters, bias, and density).

Following Sailer et al. (2021), the effective redshift of a subsample is calculated with

$$z_{\rm eff} = \frac{\int dz H^2(z)\chi^2(z)(d\chi/dz)^3 n^2(z) z}{\int dz H^2(z)\chi^2(z)(d\chi/dz)^3 n^2(z)}. \quad (16)$$

None of these approaches is flawless, and we will choose the best one for different purposes in the following study. Bailoni, Spurio Mancini & Amendola (2017) have implemented a multibins approach and show that in some case, the cross-correlation between bins modifies the forecast up to 10–20 per cent. None the less, Sailer et al. (2021) have shown that for these high-redshift galaxy surveys, the correction was negligible (<10 per cent, cf. appendix B of their paper). Zhao et al. (2019) have calculated the optimal redshift-weighting scheme for the BOSS survey and a similar algorithm can be implemented for future surveys, but this is beyond the scope of this study.

3.4 Cosmological parameters

3.4.1 BAO

For the BAO forecast, the two parameters are $\ln(D_{\rm A}/s)$ and $\ln(sH)$, with s the sound horizon, $D_{\rm A}$ the angular distance, and H the Hubble parameter. We assume to have a very good measurement of s from CMB, so that $\sigma(D_{\rm A}/s) = \sigma(D_{\rm A})/s$ and $\sigma(sH) = s\sigma(H)$, thus:

$$\sigma(\ln(sH)) = \frac{\sigma(H)}{H}; \;\; \sigma(\ln(D_{\rm A}/s)) = \frac{\sigma(D_{\rm A})}{D_{\rm A}}. \quad (17)$$

The distance error on both of the parameters is derived with the Seo & Eisenstein (2007) approximation of the Fisher matrix,

$$\mathcal{F}_{ij} = V_{\rm sur} A_0^2 \int_0^1 d\mu \int_0^\infty dk \Bigg\{ f_i(\mu) f_j(\mu) k^2 \times \frac{\exp\left(-2\,(k\Sigma_s)^{1.4}\right)}{\left(\frac{P(k)}{P(0.2)} + \frac{1}{nP(0.2)}\right)^2} \exp\left(-k^2(1-\mu^2)\Sigma_\perp^2 - k^2\mu^2\Sigma_\parallel^2\right) \Bigg\}, \quad (18)$$

where

$$f_i(\mu) = \begin{cases} \mu^2 - 1 & \text{if } i = 1; \\ \mu^2 & \text{if } i = 2. \end{cases} \quad (19)$$

$\Sigma_\parallel$ and $\Sigma_\perp$ are the root-mean-square displacement along and perpendicular to the line of sight. $\Sigma_\parallel = \Sigma_0 D(z)(1 + f(z))$ and $\Sigma_\perp = \Sigma_0 D(z)$ with $\Sigma_0 = 10.4\sigma_8\, h^{-1}$Mpc.[10] The Silk-damping effect is included with the Silk-damping scale Σ_s, expressed in h^{-1}Mpc via

$$\Sigma^{-1} = 1.6\left(\Omega_b h^2\right)^{0.52}\left(\Omega_m h^2\right)^{0.73}\left[1 + \left(10.4\Omega_m h^2\right)^{-0.95}\right] h^{-1}. \quad (20)$$

We assume a reduction of the BAO damping scale by a factor 0.5 w.r.t. the value from Seo & Eisenstein (2007), following section 4.1 of Font-Ribera et al. (2014). We fixed $A_0 = 0.55$, the WMAP3 value given in Seo & Eisenstein (2007).[11]

Here for BAO measurements in the two-tracer case, we will assume two independent measurements, and simply sum the two Fisher matrices.

3.4.2 RSD effects

We follow White, Song & Percival (2009) for the redshift space distortions forecast. For one tracer, we rewrite the equation of the power spectrum:

$$P(k, z) = \left(b(z)\sigma_8(z) + f(z)\sigma_8(z)\mu^2\right)^2 \frac{P_{\rm m}(k, z=0)}{\sigma_8(z=0)^2}. \quad (21)$$

We introduce our parameters: $\ln[b(z_i)\sigma_8(z_i)]$ and $\ln[f(z_i)\sigma_8(z_i)]$. For simplicity, we drop the explicit redshift dependence. In this case, the derivatives of power spectrum w.r.t. parameters are

$$\frac{\partial \ln P}{\partial \ln(b\sigma_8)} = \frac{2b\sigma_8}{b\sigma_8 + f\sigma_8\mu^2} \quad (22)$$

$$\frac{\partial \ln P}{\partial \ln(f\sigma_8)} = \frac{2f\sigma_8\mu^2}{b\sigma_8 + f\sigma_8\mu^2}. \quad (23)$$

Everything is similar for the case of two tracers A and B, except that we have three sets of parameters: $\ln[b_{\rm A}(z_i)\sigma_8(z_i)]$, $\ln[b_{\rm B}(z_i)\sigma_8(z_i)]$, and $\ln[f(z_i)\sigma_8(z_i)]$, with additional derivatives:

$$\frac{\partial \ln P_{\rm A}}{\partial \ln(b_{\rm B}\sigma_8)} = \frac{\partial \ln P_{\rm B}}{\partial \ln(b_{\rm A}\sigma_8)} = 0, \quad (24)$$

$$\frac{\partial \ln P_{\rm AB}}{\partial \ln(b_x\sigma_8)} = \frac{b_x\sigma_8}{b_x\sigma_8 + f\sigma_8\mu^2} \quad (25)$$

[9] Surveys with non-overlapping redshift ranges, sky coverages, or independent tracers.

[10] The value in Seo & Eisenstein (2007) for Σ_0 is different since we chose to work with $D(z)$ instead of $G(z)$,and we chose a different σ_8 value.

[11] We have tried varying A_0 between 0.45 and 0.6, the resulting difference on $\sigma(H)$ and $\sigma(D_A)$ w.r.t. $A_0 = 0.55$ was about 10 per cent, which is not significant for our work.

$$\frac{\partial \ln P_{AB}}{\partial \ln(f\sigma_8)} = f\sigma_8\mu^2 \left(\frac{1}{b_a\sigma_8 + f\sigma_8\mu^2} + \frac{1}{b_b\sigma_8 + f\sigma_8\mu^2} \right), \quad (26)$$

where $x = \mathrm{A}, \mathrm{B}$.

3.4.3 Non-Gaussianity

In most NG model (Matarrese et al. 2000; Maldacena 2003; Dalal et al. 2008; Desjacques et al. 2009), the Bardeen potential is assumed to contain a quadratic Gaussian field ϕ contribution $\Phi = \phi + f_{\rm NL}(\phi^2 - \langle\phi\rangle^2)$. The quadratic term induces a non-Gaussian perturbation to the bias: $b(k, z) = b_G(z) + \Delta b(k, z)$ with:

$$\Delta b = 3 f_{\rm NL}(b_G - p)\delta_c \frac{\Omega_m}{k^2 T(k) D(z)} \left(\frac{H_0}{c} \right)^2. \quad (27)$$

$f_{\rm NL}$ is the NG coupling to evaluate, $T(k)$ is the transfer function (with $k^2T(k)$ normalized to 1 at large scales), and p is a number that theoretically depends on the tracer type, and was introduced to show deviations from the original model of Dalal et al. (2008). We take $f_{\rm NL} = 0$ as a fiducial value. Since p is not well characterized yet, we will assume $p = 1$ for all the different tracers. The lack of knowledge on p value will be discussed in Section 4. We consider two parameters for the forecast $\{b_g, f_{\rm NL}\}$, with

$$\frac{\partial P}{\partial f_{\rm NL}} = 2\frac{\partial \Delta b}{\partial f_{\rm NL}}(b_G + \Delta b + f\mu^2)P_{\rm m}(k). \quad (28)$$

For the generalization to two tracers, there is an additional derivative

$$\frac{\partial P_{\rm AB}}{\partial f_{\rm NL}} = \frac{\partial \Delta b_a}{\partial f_{\rm NL}}(b_b + \Delta b_b + f\mu^2)P_{\rm m}(k) + \{b \leftrightarrow a\}. \quad (29)$$

Karagiannis et al. (2018) and Ferraro & Wilson (2019) have suggested that by using bispectrum in addition to the power spectrum, one might be able to reach $\sigma(f_{\rm NL}) \sim 0.1$. The modelling of bispectrum observations is relatively complex, and this high-precision constraint requires indeed more theoretical development from the modelling side, as well as better understanding of systematics effects (Yankelevich & Porciani 2019). Our study is far too simplistic to address these issues, so we leave it for future studies.

3.4.4 Neutrino mass

The evaluation of the sum of the NM is an active subject, both in cosmology and in particle physics. We adopt a linear power spectrum Fisher approach. It may seem too simple to the current standard algorithm, which consists of forecasting with an MCMC and non-linear corrections in the model (e.g. Sailer et al. 2021). However, our aim in this paper is to study the change of constraints w.r.t. that of observational parameters in spectroscopic surveys. Furthermore, even the most advanced approaches do not agree with each other (an issue discussed in Boyle 2019). Indeed, we expect that the difference between our power spectra and those provided by a more complex M_ν will be relatively similar for all surveys and our conclusion should not be affected.

The sum of NM is denoted as

$$M_\nu = \sum_\nu m_\nu. \quad (30)$$

We consider a cosmology described by the six standards cosmological parameters and M_ν,

$$\{p_i\} = \{M_\nu, H_0, \omega_c, \omega_b, \tau, n_s, A_s\}. \quad (31)$$

Table 3. The redshift slices and the mean number density at that redshift range for DESI tracers.

Tracers	Redshift Range	n ($10^{-4}\,h^3\,\mathrm{Mpc}^{-3}$)
LRG	0.65–1.05	3.0
ELG	0.75–1.05	9.8
	1.05–1.35	4.5
	1.35–1.65	1.3
QSO	1.96–2.43	0.17
	2.43–3.55	0.063

To evaluate the derivative of the power spectrum w.r.t. these parameters, we use a 4-point estimate (we drop the k, z, μ dependency here):

$$\frac{\partial P}{\partial \theta}|_{\theta_{\rm fid}} \sim \frac{-P(\theta+2\delta\theta)+8P(\theta+\delta\theta)-8P(\theta-\delta\theta)+P(\theta-2\delta\theta)}{12\delta\theta}. \quad (32)$$

We use $\delta\theta/\theta = 0.01$ except for $\delta\tau/\tau = 0.5$ and $\delta M_\nu/M_\nu = 0.05$ for numerical reasons. Indeed, we want the power spectrum variation (for every step) to be much larger than this numerical noise induced by solving Boltzmann equations. Thus, for parameters that have only a small impact on the matter power spectrum (the NM M_ν, and the optical depth τ), we take a larger parameter step size. We pay particular attention to the numerical stability and convergence of the derivatives w.r.t. those steps. We fix the neutrino hierarchy as it is degenerated in CAMB, for numerical error purposes.

One subtlety not always mentioned is that the power spectrum used in M_ν study includes only baryons and cold dark matter and its associated growth rate f. Indeed, neutrino perturbations do not contribute to the formation of galaxies and haloes (Boyle 2019). We focus on the NM parameter and marginalized our Fisher matrix over all the other parameters.

3.4.5 Additional data sets for NM

We will add a prior, using Planck CMB constraints on our standard set of parameters: $(F^{\rm Planck})_{ij} = \delta_{ij}/\sigma_i^2$ (Section 3.3.3 and Table 2). We will also consider the possibility of combining our forecast with DESI, which has three tracers: ELG, LRG, and QSO. We split DESI, ELG, and QSO into several redshift bins and sum the corresponding Fisher matrix as

$$F^{\rm DESI} = F^{\rm DESI}_{\rm LRG} + F^{\rm DESI}_{\rm ELG} + F^{\rm DESI}_{\rm QSO}, \quad (33)$$

neglecting the correlation between bins. We also neglect cross-correlation between tracers. Table 3 summarizes the redshift binning of DESI tracers. Since our goal is not to derive the optimal bound, but rather to make comparisons among different surveys, we do not include additional information for BOSS or Euclid for example. The argument is similar to the one for NM modelling.

3.5 High-redshift survey modelling

In this section, we model a general survey (cf. Section 2.5), keeping engineering and observational parameters as variables. We will then investigate the survey characteristics to get the best constraint on parameters $f_{\rm NL}$ and M_ν.

3.5.1 Time to observe a single galaxy

The signal-to-noise ratio (SNR) describes how well a source is measured by an instrument. In the case of a Charge Coupled Device (CCD) the SNR is given by the CCD equation,

$$S/N \sim \frac{I(m)S_{\rm tel}t}{\sqrt{I(m)S_{\rm tel}t + \epsilon_{\rm sky} + \epsilon_{\rm read}}}, \tag{34}$$

with $S_{\rm tel}$ the telescope surface, t the time of observation, and $I(m)$ the luminous flux from the source. $\epsilon_{\rm sky}$ and $\epsilon_{\rm read}$ are sky noise and read-out noise, which we can neglect in our study since we are dealing with the deep sky. Thus we have

$$S/N \sim \sqrt{I(m)S_{\rm tel}t}. \tag{35}$$

During a telescope operation phase, the time for observing an object is fixed to the exposure time $t_{\rm exp}$, independently of its apparent magnitude. After a first exposure, the spectrum might still be too noisy to identify lines for determining the redshift. That defines the first exposure magnitude efficiency $p(m|t_{\rm exp})$, which is the probability of getting a redshift-identifiable spectrum during $t_{\rm exp}$.

3.5.2 One exposure

For a single exposure of $t_{\rm exp} = 1800\,s$, with a telescope of diameter $\sim 10\,m$, we assume that

$$p(m|t_{\rm exp}) = E(m), \tag{36}$$

where $E(m)$ is the observational efficiency introduced in Section 2.2 for the modelling of MSE efficiency (Percival et al. 2019). This law depends on the exposure time $t_{\rm exp}$, the telescope surface $S_{\rm tel}$, the maximum tolerable redshift error $|z_{\rm meas} - z_{\rm real}| = 0.001(1 + z_{\rm real})$, and spectra simulated with the MSE exposure time calculator, given the redshift finder PandoraEZ (Fumana & Garilli 2012). Furthermore, this law is based on the assumptions of LBG properties that half of LBG have a detectable Ly α emission line, and the redshift of the other half can be estimated with their Ly α and Ly β absorption features. Thus, except for the exposure time, and telescope surface, this law is not specific to MSE survey and should in principle apply to other spectroscopic surveys.

3.5.3 Multiple exposures

After a first exposure, if the spectrum is still too noisy, a target may get another exposure $t_{\rm exp}$.

We assume that if one observes an object with an additional exposure after a first failure, the probability of measuring its redshift accurately from the stacked spectrum is

$$p(m|2t_{\rm exp}) = \sqrt{2}p(m|t_{\rm exp}). \tag{37}$$

Indeed, in Appendix A, we show that the efficiency of the ELG detection increases linearly with the SNR for eBOSS ELGs, up to a very good precision. Thus, we assume a similar trend for high-redshift LBGs, i.e. the efficiency is proportional to the SNR and scales with $\sqrt{t}$ according to equation (35). If we go even further and decide to attribute the third exposure of two failures, we assume $p(m|3t_{\rm exp}) = \sqrt{3}p(m|t_{\rm exp})$ and so on.

3.5.4 Correcting efficiency bias

The one-exposure efficiency of fainter tracers is significantly smaller than that of bright objects, and one will underestimate the proportion of high-magnitude tracers. As a consequence, the sample will be biased to large $m_{\rm max}$. That is why we define a minimal observational efficiency $p_{\rm min}$ so that $\forall m < m_{\rm max},\ p(m) \geq p_{\rm min}$. In practice, we decide to attribute a second exposure after the first failure to a certain fraction of object: η_2, with $0 \leq \eta_2 \leq 1 - E(m)$ (we assign only a second observation if the first exposure failed). We also define the fraction of object observed once η_1, with $E(m) \leq \eta_1 \leq 1$. Similarly, if observing all objects that failed during the first exposure twice does not compensate for the efficiency decreased, a fraction of galaxies η_3 might need a third observation. This procedure defines an efficiency law[12]: $p(m) = \max(E(m), p_{\rm min})$. As an example, in Fig. 1 we fix $p_{\rm min} = 0.7$ and we plot $p(m)$ (solid line), as well as $E(m)$ (dashed line), as functions of apparent magnitude m. For $m < m_1 = 22.8$, we have $p(m) = E(m)$; $p(m) = p_{\rm min}$ for higher magnitude. In the same figure, we also represent in colour the different fractions of galaxy observed n times η_n, as a function of apparent magnitude m, with $\sum_n \eta_n(m) = 1$. The fraction of objects that have been correctly observed during the first exposure[13] is equal to $E(m)$ by definition. For $m < m_1$, $E(m) > p_{\rm min}$, and all the object are observed once: $\eta_1(m < m_1) = 1$. For $m_1 < m < m_2$, to compensate that $E(m) < p_{\rm min}$, a fraction η_2 of galaxy is observed twice (the green shade). Then at $m = m_2$, we have $\eta_1 = E(m_2)(= 0.37)$, which means that all the objects whose observation failed during the first exposure are observed twice (so 63 per cent of the sample). Thus for $m > 24.6$, some galaxies might need a third observation (blue shade) to compensate for the gap between $E(m)$ and $p_{\rm min}$. With our model, for efficiency $p_{\rm min} < 0.85$, it is never necessary to observe some object four times.

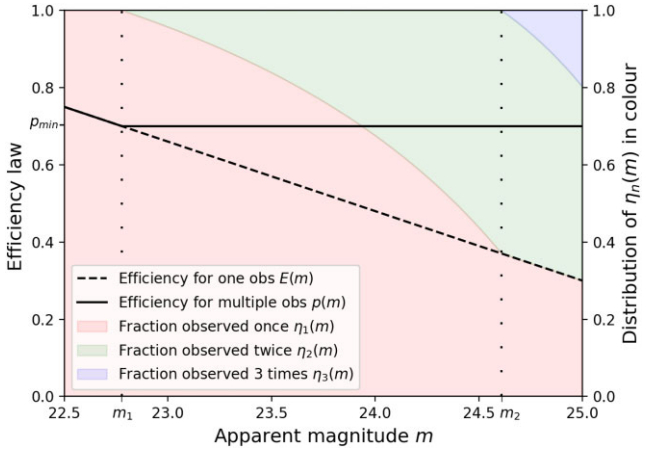

Figure 1. Efficiency law for a single exposure $E(m)$ (dashed line) and for multiple exposures $p(m)$ (solid line), with a minimal efficiency $p_{\rm min} = 0.7$ (reported on the y-axis on the left) as a function of apparent magnitude m. Colours represent the fraction of galaxies of magnitude m that have been observed n times: $\eta_n(m)$, with $\sum_n \eta_n(m) = 1$. Values of these fractions are deduced from the y-axis on the right. For e.g. at $m = 25$, 30 per cent of galaxies are observed once, 50 per cent are observed twice, and 20 per cent are observed three times. We have also reported two particular magnitudes m_1 and m_2 by vertically pointed lines.

The average time dedicated to the observation of an object of magnitude m (whether it is a success or not) is

$$\langle t(m) \rangle = \sum_n \eta_n(m) \cdot n \cdot t_{\rm exp}. \tag{38}$$

[12] We neglect the bias induced by the high efficiency of low-magnitude sources.

[13] Which is not $\eta_1(m)$.

The analytical expressions of η_n and $\langle t(m)\rangle$ as function of $p_{\rm min}$, $E(m)$, and m are given in Appendix B.

3.5.5 *Survey duration and measured density*

The observed volume is described by three numbers: $z_{\rm min}$, $\Delta z = z_{\rm max} - z_{\rm min,}$ and $f_{\rm sky}$. From all available galaxies within this volume, we will visit a fraction $\eta_{\rm til} \lesssim 1$ of them, and the visited tracer number is:

$$N_{\rm vis} = \eta_{\rm til} \int_{z_{\rm min}}^{z_{\rm max}} dz \frac{d\chi}{dz} 4\pi f_{\rm sky} \chi^2 \int^{m_{\rm max}} dm \phi_{\rm LBG}(z, m). \tag{39}$$

This equation is the integration of the number density over the cosmic volume. The $\eta_{\rm til}$ factor takes into account two effects:

(i) The fibre collision: two close tracers cannot be observed simultaneously by two fibres during a single exposure.
(ii) The tilling: the sky is generally not perfectly covered by the succession of focal planes, if objects are attributed to different exposures by maximizing the survey efficiency, which is typically the case in reality.

From this last equation, we further define the density of visited tracer per magnitude,

$$dN_{\rm vis}(m) = 4\pi f_{\rm sky} \eta_{\rm til} \int_{z_{\rm min}}^{z_{\rm max}} dz \frac{d\chi}{dz} \chi^2 \phi_{\rm LBG}(z, m) dm. \tag{40}$$

Given the average time to observe a tracer with magnitude m $\langle t(m)\rangle$ [cf. equation (38)], and the fibre number $N_{\rm fib}$, the total observational time of the survey is

$$\begin{aligned} \alpha T_{\rm sur} &= \int^{m_{\rm max}} dN_{\rm vis}(m) \langle t(m)\rangle / N_{\rm fib} \\ &= \eta_{\rm til} \frac{4\pi f_{\rm sky}}{N_{\rm fib}} \int_{z_{\rm min}}^{z_{\rm max}} dz \frac{d\chi}{dz} \chi^2 \int^{m_{\rm max}} dm \langle t(m)\rangle \phi_{\rm LBG}(m, z), \end{aligned} \tag{41}$$

where $T_{\rm sur}$ is the total survey duration (typically 5 yr), and α is a coefficient to convert it into observational time. For cosmological observations, we assume that we observe only days with a partial moon[14], 21 d every 28 d cycle, within practice only 80 per cent of these nights that can be dedicated to observation (due to weather or maintenance issues)[15], and between 8 and 10 h of observation per night, which correspond to $\alpha = 7 \times 10^6\,{\rm yr}^{-1}{\rm s}$. In equation (41), we are assuming that every fibre is dedicated to observation and will be observed during every exposure.

The density of observed tracers with a good spectroscopic redshift is

$$n_{\rm obs}(z) = \eta_{\rm til} \int^{m_{\rm max}} dm p(m) \phi_{\rm LBG}(m, z). \tag{42}$$

Since $T_{\rm sur} \propto 1/N_{\rm fib}$, the observation for a 5-yr survey with 20 k fibre would be equivalent to that of a 10-yr survey with 10 k fibres. Thus, we introduce the 'power' parameter $N_{\rm fib}\,T_{\rm sur}$ in fibre-year.

3.5.6 *Optimization pipeline*

In the first part of our general survey study, we fix the following parameters:

[14]Days with a full moon can be thus fully dedicated to other astrophysical observation.
[15]For 5 yr, this corresponds to ≈1100 nights.

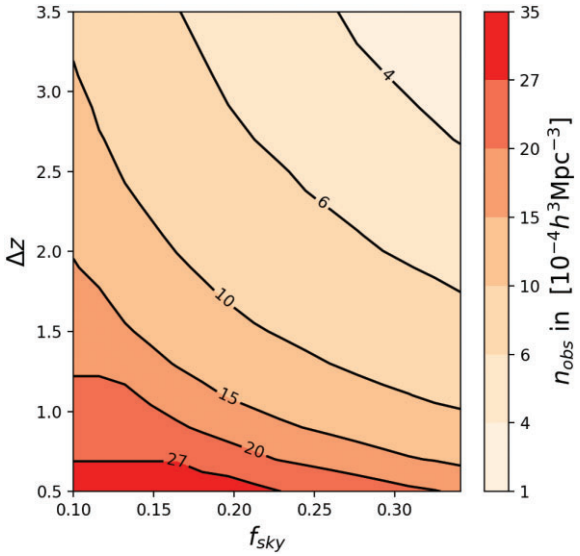

Figure 2. Observed density $n_{\rm obs}$ as a function of the redshift width Δz and the sky coverage $f_{\rm sky}$, for $N_{\rm fib}\,T_{\rm sur} = 100\,000$ fibre-years, $z_{\rm min} = 2$, and $p_{\rm min} = 0.7$. We observe hyperbolic trends, with saturation in the small volume region (bottom left corner), visible with the 20 and 27 $\times\ 10^{-4}h^3{\rm Mpc}^{-3}$ lines.

(i) $N_{\rm fib}\,T_{\rm sur} = 100,000$ in fibre-year; it corresponds to 5 yr of observation with 20 000 fibres for example;
(ii) $\eta_{\rm til} = 0.96$, is the fraction of available tracer in our cosmic volume that we will observe;
(iii) $t_{\rm exp} = 1800\,{\rm s}$ is the exposure time of the instrument;
(iv) $p_{\rm min} = 0.7$ is the minimal efficiency rate;
(v) $z_{\rm min} = 2$ is the minimal redshift of our high-redshift surveys;
(vi) $\alpha = 7 \times 10^6$, as explain in Section 3.5.5;
(vii) the telescope size to be 10 m;

and find the optimal survey volume described by:

(i) $f_{\rm sky}$, the observed fraction of the sky, and
(ii) $\Delta z = z_{\rm max} - z_{\rm min}$, the redshift width.

For arbitrary values of these two parameters, equations (41) and (42) will constrain:

(i) $m_{\rm max}$ the maximal magnitude of observation,
(ii) $n_{\rm obs}(z)$ the tracer density,

according to the following scheme,

$$f_{\rm sky},\ \Delta z \xrightarrow{\text{Eq. (41)}} m_{\rm max} \xrightarrow{\text{Eq. (42)}} n_{\rm obs}(z) \xrightarrow{\mathcal{F}_{ij}} \sigma(f_{\rm NL}), \sigma(M_\nu). \tag{43}$$

The numerical procedure to get $m_{\rm max}$ is explained in Appendix C.

In the second step, we fix the optimal survey volume, and free $N_{\rm fib}\,T_{\rm sur}$ and $p_{\rm min}$ in a similar procedure as previously, mainly for two reasons. First, it will show the optimal strategy between correctly measuring most of the objects visited (high $p_{\rm min}$), or having a wider magnitude range and observing fainter objects that are located in the high-redshift region. Secondly, it will quantify the improvement of the data over the fibre number and the duration of the survey. We will vary $N_{\rm fib}\,T_{\rm sur}$ from 60 000 to 220 000 fibre-years.

3.5.7 *Observed density prediction*

Before moving on to the cosmological parameters, we show here some results of our modelling. We plot Fig. 2, the measured tracer density $n_{\rm obs}$ as a function of the survey cosmic volume, with

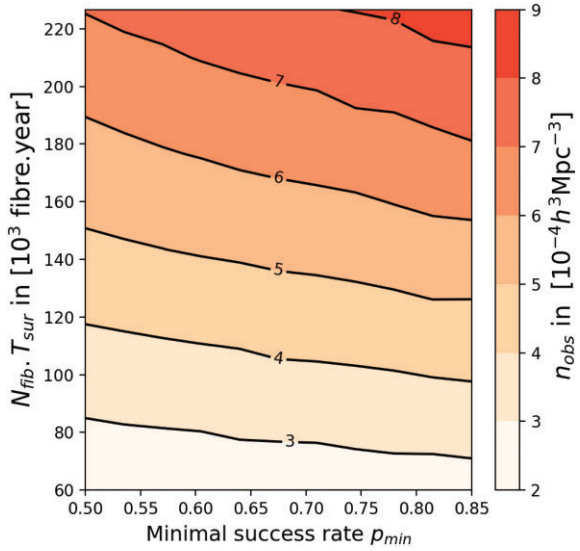

Figure 3. Observed density $n_{\rm obs}$ as a function of $N_{\rm fib}T_{\rm sur}$, and minimal efficiency $p_{\rm min}$, for a maximal cosmic volume: $f_{\rm sky} = 0.31$, $\Delta z = 3$, and $z_{\rm min} = 2$). The density increases linearly as a function of $N_{\rm fib}.T_{\rm sur}$, and increases with the efficiency threshold.

parameters described in Section 3.5.6 [first two steps of equation (43)].

We observe hyperbolic trends, as expected since the product of the two variables scales as the volume at first order (naive model). For small volumes (e.g. $f_{\rm sky} = 0.15$ and $\Delta z = 0.7$), the maximum magnitude of 25 is reached (as illustrated by horizontal lines), and all tracers are visited by the end of the 5th yr, which leads to saturation (cf. Appendix C). We also plot in Fig. 3 the average density as a function of $N_{\rm fib}\,T_{\rm sur}$ and the minimal efficiency $p_{\rm min}$. For a fixed $N_{\rm fib}\,T_{\rm sur}$, the density of observed tracers $n_{\rm obs}$ will be higher with higher minimum efficiency $p_{\rm min}$. Indeed, if an observation of a magnitude m_1 object failed in the first exposure, then its second-exposure observation is more likely to be successful than a first-exposure observation of another object of magnitude $m_2 \geq m_1$[16] None the less, with lower minimal efficiency, the maximal magnitude is higher and one is observing more objects at higher redshift. Thus, it is a priori difficult to know which strategy will provide the best constraints on the cosmological parameters.

With this general survey model, one should be able to reproduce fiducial tracer properties of future surveys with known observational parameters such as MegaMapper. It is a large-volume survey with $f_{\rm sky} \sim 0.3$ and $\Delta z = 3$ but with a smaller telescope diameter (~6.5 m) than the one assumed for $E(m)$ (cf. Section 3.5.2). Motivated by the dependence of the CCD equation (35) on $\sqrt{S_{\rm tel}}$, we correct the efficiency law $E(m)$ by a factor $\sqrt{S_{\rm Mega}/S_{\rm MSE}}$ and require a minimum efficiency $p_{\rm min} = 0.5$ (Section 2.1). The predicted number density is $n_{\rm obs} \sim 2.6 \times 10^{-4}\,h^3\,{\rm Mpc}^{-3}$, very close to the expectation of MegaMapper, which is $2.5 \times 10^{-4}\,h^3\,{\rm Mpc}^{-3}$. The maximum magnitude imposed by the model is 24.6, which is in agreement with MegaMapper's 24.5 maximal magnitude. It should be noted that this agreement is remarkable since our modelling is independent of any MegaMapper settings.

[16]Indeed, during the second exposure, the initial SNR value will be the one obtained at the end of the first exposure.

4 RESULTS

In this section, we first present the BAO, RSD, NG, and NM forecasts for future surveys such as MUST, MegaMapper, and MSE. We then investigate the NM and NG accuracy, given the survey properties with our model introduced in Section 3.5. We deduce, independently of any planned survey, the optimal observation strategies and the limits when measuring these parameters.

4.1 BAO and RSD constraints

We summarized in Table 4 the constraints on BAO and RSD parameters. We separate MegaMapper and MSE redshift range into several bins and present the forecast for every bin. We also provide constraints in the full redshift range in the last row for each survey. We derived the constraints for eight different settings of MUST, and for three different settings of an NTL survey, that mimics the observation of the WST survey (depending on the fibre number). Finally, we consider a combination of two MegaMapper-like surveys, each located in one hemisphere. This study shows the power of combined independent surveys in providing better cosmological constraints.

From this table, we can conclude that:

(i) MegaMapper and MUST (20 000 fibres) have relatively similar accuracy. In theory, they will improve the constraints on BAO and RSD by a factor of 10 w.r.t. eBOSS constraints (Zhao et al. 2016), and a factor between 2 and 3 w.r.t. DESI constraints (DESI Collaboration et al. 2016). MSE forecasts are not as good as these two because of its smaller fibre number.

(ii) For MUST, with the same number of fibre, the one-tracer (LBGX) case gives better constraints than the two tracers (LBGX + LAE) one. It is mainly because LAEs need a long exposure time, which decreases the total number of observed LAEs and thus increases the overall noise, as illustrated by the nP parameter values.

(iii) The combination of two independent LBG surveys gives cosmological constraints similar to those of an NTL survey with 40 000 fibres, a factor of $\sqrt{2}$ smaller than those of a single survey like MegaMapper. As the two surveys are independent, this corresponds to the constraints on the BAO and RSD from two independent measurements, combined.

(iv) 100 000 fibres in the NTL survey represent the upper limit for these high-redshift LBG surveys since it corresponds to the measurement of all galaxies up to $m_{\rm max} = 25$.

(v) All the parameters are very well constrained down to the sub-per cent level in every survey. This is unrealistic as the real observational constraints are likely to be dominated by systematics and not anymore by the number density of tracers and the cosmic volume.

As the sample size will not bring improvement for cosmological measurements of future surveys, we do not optimize it in the following study.

4.2 Non-Gaussianity and NM

4.2.1 Redshift binning

As mentioned in Section 3.3.4, there are several ways to deal with the large cosmic volume. In Section 4.1, as their parameters are redshift-dependent, it is natural to provide forecasts in small redshift bins. In contrast, non-Gaussianity and NM are independent of the redshift. Thus, splitting the samples into multiple redshift bins does not bring

Table 4. The predicted 68% confidence level (CL) error of the BAO distances and RSD parameters for various surveys. We use separate redshift bins for MegaMapper and MSE, and we also show the forecast using tracers at the whole redshift range in the last row of each survey. We present the forecast for MUST at $2 < z < 4$ and for NTL and combined surveys at $2 < z < 5$. LBGX × LAE denotes a multitracer constraint with LBGX and LAE.

				BAO and RSD forecast					
Fibre number	Sky area deg^2	Tracer	Redshift	Number density $10^{-4}\,h^3\,\mathrm{Mpc}^{-3}$	$nP(0.14, 0.6)$	$\sigma(D_A)/D_A$ (%)	$\sigma(H)/H$ (%)	$\sigma(b\sigma_8)/b\sigma_8$ (%)	$\sigma(f\sigma_8)/f\sigma_8$ (%)
MegaMapper									
20k	14k	LBG	$2 < z < 2.5$	7.9	1.7	0.32	1.0	0.066	0.85
			$2.5 < z < 3$	3.6	0.68	0.35	1.0	0.073	1.0
			$3 < z < 4$	1.1	0.19	0.40	1.0	0.085	1.3
			$4 < z < 5$	0.7	0.11	0.45	0.99	0.094	1.7
			$2 < z < 5$	2.5	0.5	0.18	0.57	0.039	0.52
MSE									
4.3k	10k	ELG	$1.6 < z < 2.4$	1.8	0.28	0.86	2.5	0.17	1.4
		LBG	$2.4 < z < 2.8$	2.3	0.51	0.51	1.5	0.10	1.7
		LBG	$2.8 < z < 3.2$	1.1	0.22	0.66	1.8	0.14	2.3
		LBG	$3.2 < z < 4$	0.43	0.08	0.79	1.9	0.17	2.8
		LBG	$2.4 < z < 4$	1.1	0.28	0.28	0.64	0.078	1.2
MUST (different settings)									
20k	15k	LBGX	$2 < z < 4$	8.9	2.3	0.13	0.41	0.026	0.44
20k	15k		$2 < z < 4$	4.2–0.84	1.1	0.15	0.49	0.030–0.14	0.47
		LBGX×LAE							
10k	15k	LBGX	$2 < z < 4$	5.0	1.3	0.15	0.48	0.030	0.52
10k	15k		$2 < z < 4$	2.1–0.42	0.58	0.19	0.62	0.039–0.21	0.60
		LBGX×LAE							
10k	9k	LBG	$2 < z < 4$	7.1	2.1	0.18	0.56	0.035	0.60
10k	9k		$2 < z < 4$	3.5–0.71	0.97	0.21	0.68	0.041–0.21	0.66
		LBGX×LAE							
NTL (WST-like survey)									
20k	15k	LBG	$2 < z < 5$	2.5	0.51	0.15	0.48	0.035	0.54
40k	15k	LBG	$2 < z < 5$	4.9	0.99	0.12	0.38	0.030	0.40
100k	15k	LBG	$2 < z < 5$	13	1.9	0.099	0.29	0.027	0.26
Combination of two MegaMapper-like surveys									
20k	28k	LBG	$2 < z < 5$	2.5	0.5	0.13	0.40	0.028	0.37

more information for their measurements in principle. However, as the number density of tracers is much higher at low redshift than that at high redshift, analysing the total redshift range is not necessarily the best option. Because it may overestimate the noise that scales as $1/n$ at low redshift.

We, therefore, investigate the optimal binning by exploring two ways to separate our redshift interval $[z_{\min}, z_{\max}]$ into $N_{\rm bins}$:

(i) Define bins with the same comoving volume V: a 'fixed volume approach'.

(ii) Define bins with the same number of targets $N_{\rm gal}$. In this case, the low-redshift bins have volumes smaller than those at higher-redshift bins.

A model including a continuous dependence of the redshift and density is more promising, but we leave this more complex option for a future study. We calculate $\sigma(f_{\rm NL})$ and $\sigma(M_\nu)$ for $N_{\rm bins} = 1, 2,..., 10$, and report their relation in Fig. 4. We fix the tracer density and cosmic volume for these forecasts to be the fiducial MegaMapper ones. We check that the optimal binning scheme is independent of these parameters.

For non-Gaussianity, the fixed volume approach provides the best constraints with two or three bins. Indeed, $f_{\rm NL}$ describes a large-scale phenomenon, and reducing bin sizes increases the low integration limit value $k_{\min}$, which leads to a rapid increase in variances for a large number of bins. The drop in $f_{\rm NL}$ accuracy from one bin to two bins is due to the reduction in noise at the low-redshift bin, which compensates for its small volume.[17]

For NM measurement, contrary to $f_{\rm NL}$, there is no clear pattern, and therefore no number of bins has to be preferred. In fact, except for one bin, the results fluctuate by less than 5 per cent from the mean value, which is not large given our method. This is a confirmation that this forecast does not depend on large scales but on small ones as theoretically expected.

In the following studies, we adopt a volume-fixed approach with three bins for both forecasts.

4.2.2 *Small-scale choice*

We do the forecast with two different $k_{\max}$ values: 0.1 and 0.3 $h\mathrm{Mpc}^{-1}$. The $k_{\max}$ reached in the future survey analysis may be between these two, or even larger. However, for $k_{\max} = 0.3\,h\mathrm{Mpc}^{-1}$, our linear approach is already insufficient, and a proper future analysis would have to take into account non-linear correction as what Boyle & Schmidt (2021) and Sailer et al. (2021) have done. This will mainly affect the neutrino forecast since non-Gaussianity is a large-scale phenomenon, whereas the power spectrum is more affected by the massive neutrino contribution at large k.

[17]This difference is smaller in the case of the fixed number of tracer. Because in that case, the volume of the low-redshift bin is small, and we have a small bin with low noise and a large bin with high noise at high redshift.

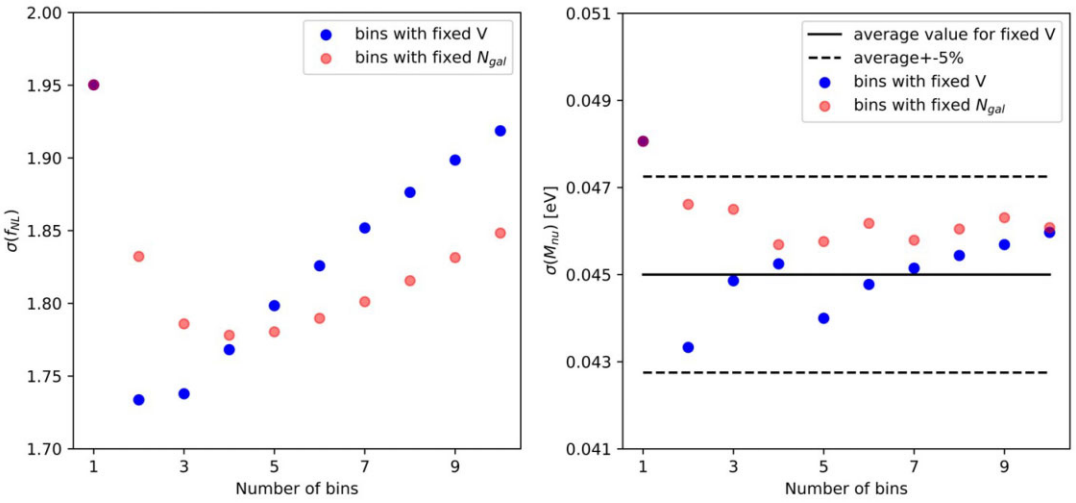

Figure 4. NM (the left panel) and NG (the right panel) forecast w.r.t. the bin number for two binning schemes (V-based in blue dots and $N_{\rm gal}$-based in pink dots). For NM, we also include the average value for the fixed volume approach (solid lines) and delimit the ±5 per cent region around it by the two dashed lines. For NG, the approach with fixed volume is clearly the optimal one with two or three bins, whereas, for NM, there is not the best choice.

4.2.3 Forecasts

In Table 5, we present forecasts for the same surveys as Table 4, but for the NM and non-Gaussianity. For the neutrino forecast, we provide constraints with only a prior from Planck CMB, and those with a Planck CMB prior and measurements from DESI, as described in Section 3.4.5.

For non-Gaussianity, we may reach with MegaMapper-like survey $\sigma(f_{\rm NL}) \sim 1.2$, which is a factor of 4 better than the DESI forecast (DESI Collaboration et al. 2016). In particular, the constraints depend mainly on the volume of the survey. For example, with the number of fibres reduced by a factor 2 (which propagates to the tracer density), constraints of MUST vary from 1.6 to 1.7 for $k_{\rm max} = 0.1h{\rm Mpc}^{-1}$, whereas reducing the observation window from 15 000 to 9000 deg^2 leads to a weaker constraint from 1.7 to 2.1 for 10 000 fibres (despite a higher tracer density for the reduced window). $k_{\rm max}$ values have little impact on $f_{\rm NL}$, which is within expectation since it describes a large-scale deviation from classical Gaussian prediction. A combination of two surveys (coverage of 28 000 deg^2) results in a smaller $\sigma(f_{\rm NL})$ than the NTL with 100 000 fibres, which shows that the measurement of this parameter is limited by the volume and not the tracer density. That is also why, MSE constraints are much weaker than the ones of the other surveys.

As already mentioned in Section 3.4.3, we assume a value $p = 1$, but indeed different values are theoretically possible. The NG amplitude is degenerated with p, as it scales as $f_{\rm NL}p$, as well as the variance. We illustrate this via the $\sigma(f_{\rm NL})$ forecast for a MegaMapper-like survey as a function of the p values in Fig. 5. In particular, for relatively reasonable values like $p = 1.6$, the variance on NG amplitude is already significantly degraded (∼30 per cent w.r.t. $p = 1$). Thus, in order to have a reliable measurement of the $f_{\rm NL}$ parameter (value and uncertainty), one needs robust theoretical priors, provided, for example, by simulations. One can find a complete discussion about this issue in Barreira (2022).

The neutrino forecast depends strongly on the value of the small-scale limit $k_{\rm max}$ (by a factor of 2 in most cases). With a CMB prior, $\sigma(M_\nu)$ values are relatively similar for most surveys of the order of 0.04eV for $k_{\rm max} = 0.1$, and 0.025eV for $k_{\rm max} = 0.3$. With our approach, we find an improvement of about 50 per cent w.r.t. CMB + DESI forecast only. Combining both, it is possible to reach 0.015 eV. However, forecasting this parameter with our naive approach aims to show global trends, and values should not be taken in the strict sense for the reasons mentioned in Section 3.4.4 but rather as indicators. Unlike the NG, the NM measurement of the combination of two surveys is worse than the NTL 100 000 fibres. Thus, this parameter is more impacted by noise.

The neutrino forecast varies slightly with the characteristics of the survey. Indeed, the limiting factor for the accuracy of this parameter is the weak prior of some parameters from the standard model, rather than the survey settings. As discussed in Boyle (2019) and Boyle & Schmidt (2021), it is due to our limited knowledge of A_s, which is linked to τ because of a strong CMB degeneracy between these two parameters.[18] table 2 of Liu et al. (2016) summarizes forecasts of the expected future knowledge on $\ln(A_s)$ and τ with future 21-cm surveys. We illustrate this issue in Fig. 6 by plotting $\sigma(M_\nu)$ for a MegaMapper-like survey, as a function of the prior on $\ln A_s$, with values credible according to table 2 of Liu et al. (2016). For example, a difference in the $\sigma(\ln A_s)$ prior from 0.014 to 0.005 leads to an improvement from 0.024eV to 0.018eV in the optimistic scenario. Thus, improving the knowledge on A_s is the best way to detect the NM hierarchy as large as a 5σ confidence level. For other cosmological parameters, we find that the dependencies are much weaker, and we simply take the CMB prior values.

4.3 Optimized NG surveys

We now study the optimized survey characteristics to minimize $\sigma(f_{\rm NL})$, with the survey model described in Section 3.5. The fixed-volume redshift bin number is given by

$$N_{\rm bin} = \begin{cases} 1 & \text{if } \Delta z < 1 \\ 2 & \text{if } 1 \leq \Delta z < 2 \\ 3 & \text{if } 2 \leq \Delta z. \end{cases} \quad (44)$$

We start this analysis by varying the cosmic volume in Fig. 7 for a survey with 100 000 fibre-years and a minimum efficiency of 0.7. The improvement of the precision goes hand in hand with the increase of the volume. Thus, for the study of $f_{\rm NL}$, one should always favour

[18] Indeed, A_s is not directly constrained but τ and $A_s \exp(-2\tau)$ are.

Table 5. The same table as Table 4 but for $f_{\rm NL}$ and M_ν. The forecast is based on a high-mode integration limit $k_{\rm max} = 0.1 - 0.3\ h{\rm Mpc}^{-1}$, which corresponds to a pessimistic and an optimistic scenario (that is why we provide two values for each parameter). The left column for M_ν is the forecast with a CMB prior, whereas the right column is the result of a combination of DESI and a CMB prior.

Non Gaussianity and neutrino mass forecast for $k_{\rm max} = 0.1$–$0.3\ h{\rm Mpc}^{-1}$							
Fibre number	Sky area deg^2	Tracer	Redshift	Number density $10^{-4}\ h^3\ {\rm Mpc}^{-3}$	$\sigma(M_\nu)$ in 10^{-2}eV Planck	$\sigma(M_\nu)$ in 10^{-2}eV Planck and DESI	
MegaMapper							
20k	14k	LBG	$2 < z < 5$	2.5	1.3–1.2	4.2–2.4	3.3–1.6
MSE							
4.3k	10k	ELG	$1.6 < z < 2.4$	1.8	8.9–8.1	5.0–4.5	4.1–3.0
		LBG	$2.4 < z < 4$	1.1	2.8–2.5	5.1–4.3	3.7–2.1
MUST (different settings)							
20k	15k	LBGX	$2 < z < 4$	8.9	1.6–1.4	4.2–2.4	3.1–1.6
20k	15k	LBGX × LAE	$2 < z < 4$	4.2–0.84	1.7–1.5	4.4–2.9	3.2–1.8
10k	15k	LBGX	$2 < z < 4$	5.0	1.7–1.5	4.3–2.8	3.2–1.7
10k	15k	LBGX × LAE	$2 < z < 4$	2.1–0.42	1.9–1.8	4.5–3.4	3.3–2.0
10k	9k	LBG	$2 < z < 4$	7.1	2.1–1.8	4.5–2.8	3.2–1.8
10k	9k	LBGX × LAE	$2 < z < 4$	3.5–0.71	2.2–2.0	4.6–3.4	3.3–2.0
NTL (WST like survey)							
20k	15k	LBG	$2 < z < 5$	2.5	1.4–1.4	4.1–2.1	3.3–1.5
40k	15k	LBG	$2 < z < 5$	4.9	1.1–1.0	3.6–1.7	3.0–1.3
100k	15k	LBG	$2 < z < 5$	13	1.0–0.90	3.2–1.3	2.7–1.0
Combination of two MegaMapper-like surveys							
20k	28k	LBG	$2 < z < 5$	2.5	0.92–0.85	3.7–1.8	3.0–1.3

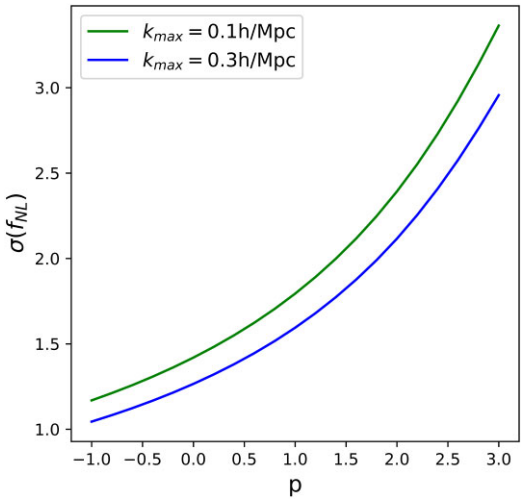

Figure 5. The predicted constraints on non-Gaussianity for a high-redshift LBG survey w.r.t. the fiducial p value.

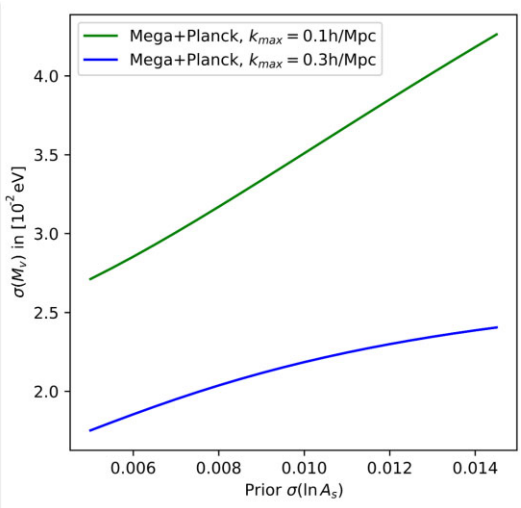

Figure 6. The predicted neutrino mass constraints for a MegaMapper-like survey w.r.t. the $\ln A_{\rm s}$ prior. For the other cosmological parameters, prior values are taken from Planck CMB measurements.

a larger survey volume. It is not beyond expectation since $f_{\rm NL}$ is a parameter related to the large scale. In addition to that, it depended little on tracer density as we show in Table 5. This remains true when varying the survey strategy parameters, such as the survey duration and the minimum efficiency.

Then, we set a maximum volume among all the surveys and vary the fibre-year parameter $N_{\rm fib}T_{\rm sur}$, as well as the minimum efficiency $p_{\rm min}$. The forecast is reported in Fig. 8. The NM accuracy depends weakly on the efficiency threshold but still deprives the high ones. Thus, it is optimal to maximize the tracer average density and to restrict the maximum magnitude of observation, as it reduces the noise. However, high-redshift bins are populated with fainter galaxies and limiting the maximal magnitude also limits the tracer density at high redshift. This mutual restriction may explain why the tendency is weak. There is also a second contribution: we consider that the effective bias is the bias of tracers with the maximum magnitude $b(z, m) \approx b_{\rm LBG}(z, m_{\rm max})$ (Section 3.2). Since bias decreases with magnitude, we underestimate the small-magnitude tracer bias. Since the NG effect scales as $\Delta b = f_{\rm NL}(b - p)$, it also reduces the amplitude of the NG.

Furthermore, multiplying the fibre-year parameter by 4 increases the accuracy only by 50 per cent. The main limitation comes neither from $N_{\rm fib}\ T_{\rm sur}$ nor from $k_{\rm max}$ but the cosmic volume of the survey $V_{\rm sur}$. However, since with a longer survey time, one is able to go to a higher magnitude, it underestimates the variance of NG amplitude because the bias decreases as described previously.

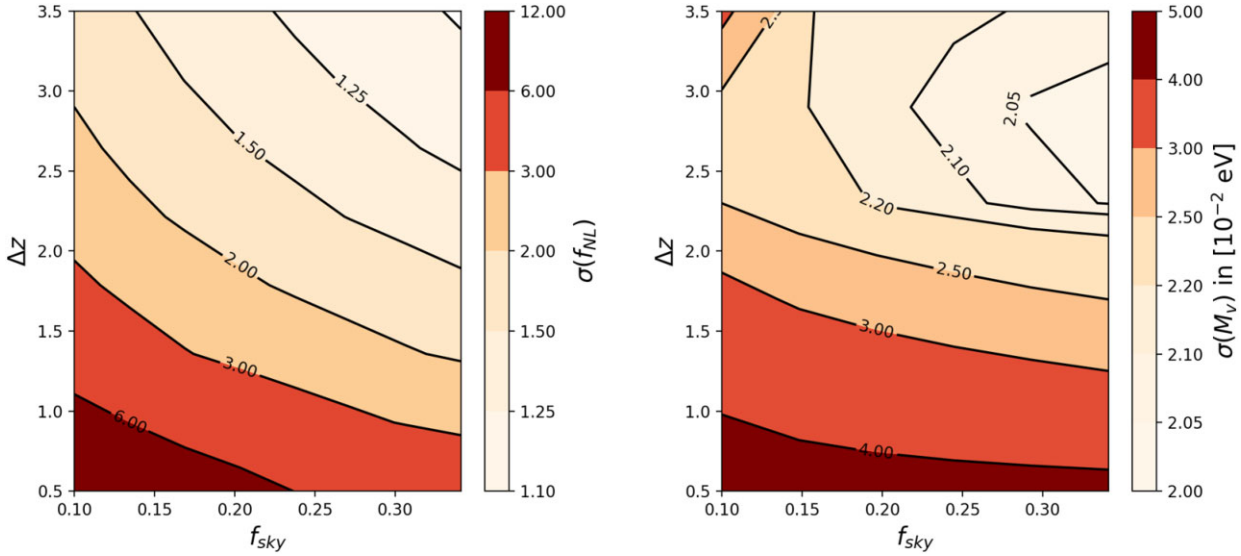

Figure 7. Non-Gaussianity (left panel) and massive neutrino (right panel) general survey forecasts as a function of the cosmic volume described by the fraction of the sky $f_{\rm sky}$ and redshift width Δz, for 100 000 fibre-year survey, $z_{\rm min} = 2$ and $p_{\rm min} = 0.7$.

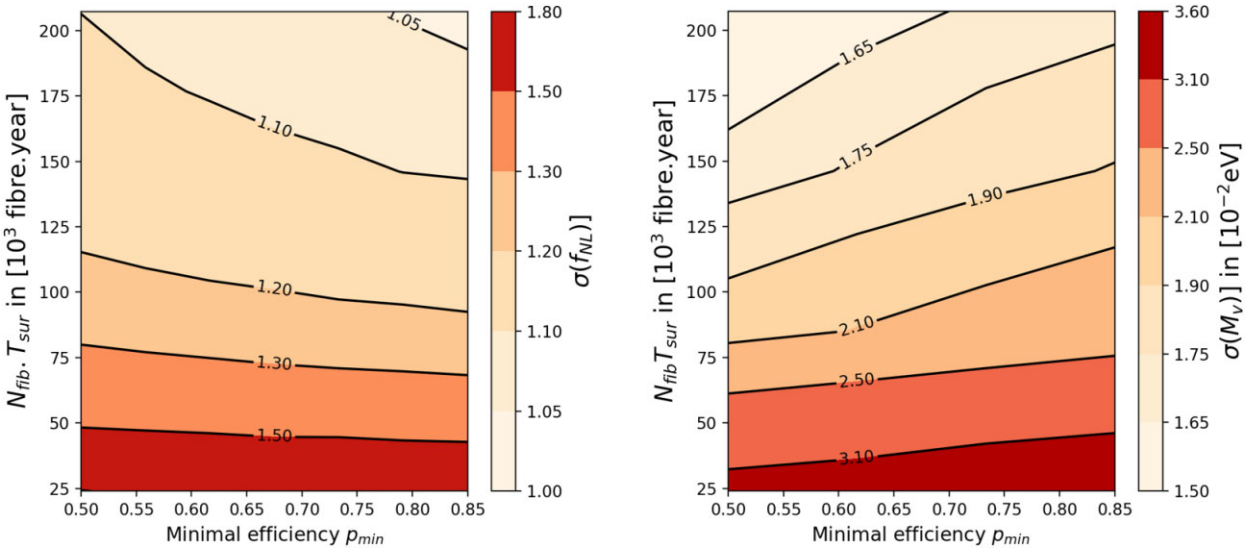

Figure 8. Non-Gaussianity (left panel) and massive neutrino (right panel) general survey forecasts as a function of the efficiency threshold $p_{\rm min}$ and $N_{\rm fib}.T_{\rm sur}$, for maximal cosmic volume: $f_{\rm sky} = 0.31$, $\Delta z = 3$, and $z_{\rm min} = 2$.

4.4 Optimized NM surveys

We adopt the same binning choice as for the NG study in Section 4.3. We first show the results for different survey volumes in Fig. 7. The variance of M_ν is less correlated with volume than for NG, especially for $f_{\rm sky}$ between 0.2 and 0.3, and Δz between 2.5 and 3.5. The optimal region seems to be around $\Delta z = 3$ and $f_{\rm sky} = 0.3$, but the variation of $\sigma(M_\nu)$ in the nearby if these parameters are comparable with the accuracy of our naive model (∼10 per cent). Thus, these results show a relatively good region, rather than a clear-cut result, with a trade-off between the volume and the noise. Furthermore, the density of LBGs at high redshift is low, and including high-redshift galaxies does not help constrain NM, given the large shot noise, beyond $\Delta z = 3$.

In accordance with the previously observed optimal region, we set the volume at $f_{\rm sky} = 0.31$ and $\Delta z = 3$. In Fig. 8, we present the forecast varying the fibre-year parameter and the minimum efficiency. The NM results are quite different from those of NG. Indeed, it is clear that the NM constraint improves with an increasing fibre-year. The error is divided by 2 when the fibre-year parameter is multiplied by 4, which means that the shot noise level plays an important role. Moreover, the best is to work with a minimum efficiency, in order to observe objects with a low luminosity, located at high redshift. We have verified that for slightly different cosmic volumes close to the maximal one, these results are unchanged.

5 CONCLUSION

As successors of DESI, MegaMapper, MSE, and MUST will become the largest spectroscopic surveys in the world in the next decades. They will map the Universe in the redshift range $2 < z < 5$ using multiple tracers and thereby improve our knowledge of cosmological distances and the structure growth (through BAO and RSD), as well as constrain the initial conditions of the Universe and measure the sum of the mass of neutrinos. It is also possible that these surveys

make observations for the $1 < z < 2$ universe. As our study focuses on high-redshift cosmology, we did not study this possibility and left it for a future article.

In this work, we find that the BAO and RSD measurements of these future surveys will reach a sub-per cent level but systematics may become dominant at some point. We show that the promising forecasts for NG ($f_{\rm NL} \sim 1$) have to be put in perspective with the lack of knowledge of the p parameter in equation (27), which could significantly degrade these results. As for the NM, most of the high-redshift studies will allow us to measure the mass up to a precision of 0.025 eV, even 0.01 eV when combined with CMB. Those tight constraints strongly depend on $k_{\rm max}$. Different surveys provide similar constraints on M_ν, and one way to significantly improve it is a better knowledge of τ and $A_{\rm s}$, using independent surveys or simulations.

In addition, we choose to model an independent general survey, described by a dozen of parameters: $\{f_{\rm sky}, z_{\rm min}, \Delta z, t_{\rm exp}, p_{\rm min}, \eta_{\rm til}, S_{\rm tel}, T_{\rm sur}, N_{\rm fib}\}$, and investigate their effects on the survey accuracy to derive the best observational strategy and the corresponding best constraints. We show that for NG, the survey volume should be maximized at the expense of the tracer density. We observe a similar trend for NM, but the increase in the sky fraction between 60 per cent and 100 per cent does not imply a significant improvement in the accuracy. There has to be a density-volume trade-off. We also illustrate that for NG, the survey duration may not significantly improve the constraint[19] and that it is better to impose a high minimum efficiency for faint objects that are crucial for mapping the high-redshift universe. The increase in the duration of the survey may significantly improve $\sigma(M_\nu)$. Furthermore, NM prefers a lower minimal efficiency, contrary to NG, so it is optimal to observe objects up to a higher magnitude. This model may be extended to investigate the nature of dark matter, the dark energy equation of state, and modified gravity. We aim at performing relevant studies in a follow-up paper.

ACKNOWLEDGEMENTS

We thank Zheng Cai for providing the expected target densities for different MUST specifications, as well as comments on the manuscript. We also thank Christophe Yeche for insightful discussions on the MSE survey properties, Noah Sailor for general discussions about spectroscopic survey forecast and Andreu Font Ribiera for his help with the NM forecast.

We acknowledge support from the Swiss National Science Foundation (SNF) 'Cosmology with 3D Maps of the Universe' research grant, 200020_175751 and 200020_207379. Work is also supported in part by the Spanish Mineco Grant PID2019-111317GB-C32. IFAE is partially funded by the CERCA program of the Generalitat de Catalunya.

DATA AVAILABILITY

Our codes are available in GitHub on open access: https://github.com/wdoumerg/Forecast_highz_spectroscopic_survey.

REFERENCES

Achúcarro A. et al., 2022, preprint (arXiv:2203.08128)
Adams J. J. et al., 2011, ApJS, 192, 5
Alam S. et al., 2021, Phys. Rev. D, 103, 083533
Annis J., Newman J. A., Slosar A., 2022, preprint (arXiv:2209.08049)
Bailoni A., Spurio Mancini A., Amendola L., 2017, MNRAS, 470, 688
Barreira A., 2022, J. Cosmology Astropart. Phys., 2022, 013
Blanchard A., Héloret J.-Y., Ilić S., Lamine B., Tutusaus I., 2022, preprint (arXiv:2205.05017)
Boyle A., 2019, PhD thesis, Ludwig-Maximilians University of Munich, Germany
Boyle A., Komatsu E., 2018, J. Cosmology Astropart. Phys., 2018, 035
Boyle A., Schmidt F., 2021, J. Cosmology Astropart. Phys., 2021, 022
Capozzi F., Lisi E., Marrone A., Montanino D., Palazzo A., 2016, Nucl. Phys. B, 908, 218
Chisari N. E. et al., 2019, ApJS, 242, 2
Chudaykin A., Ivanov M. M., 2019, J. Cosmology Astropart. Phys., 2019, 034
Copeland E. J., Sami M., Tsujikawa S., 2006, Int. J. Mod. Phys. D, 15, 1753
Dalal N., Doré O., Huterer D., Shirokov A., 2008, Phys. Rev. D, 77, 123514
Dawson K. S. et al., 2016, AJ, 151, 44
DESI Collaboration et al., 2016, preprint (arXiv:1611.00036)
Desjacques V., Seljak U., Iliev I. T., 2009, MNRAS, 396, 85
Di Valentino E. et al., 2021, Class. Quantum Gravity, 38, 153001
Douspis M., Salvati L., Aghanim N., 2019, preprint (arXiv:1901.05289)
Ellis R., Dawson K., 2019, BAAS, 51, 45
Ferraro S., Wilson M. J., 2019, BAAS, 51, 72
Font-Ribera A., McDonald P., Mostek N., Reid B. A., Seo H.-J., Slosar A., 2014, J. Cosmology Astropart. Phys., 2014, 023
Freedman W. L., 2021, ApJ, 919, 16
Fumana M., Garilli B., 2012, Astrophysics Source Code Library, record ascl:1210.004
Howlett C., Lewis A., Hall A., Challinor A., 2012, J. Cosmology Astropart. Phys., 2012, 027
Ivanov M. M., Simonović M., Zaldarriaga M., 2020, Phys. Rev. D, 101, 083504
Karagiannis D., Lazanu A., Liguori M., Raccanelli A., Bartolo N., Verde L., 2018, MNRAS, 478, 1341
Laureijs R. et al., 2011, preprint (arXiv:1110.3193)
Lesgourgues J., Pastor S., 2014, New J. Phys., 16, 065002
Liu A., Pritchard J. R., Allison R., Parsons A. R., Seljak U., Sherwin B. D., 2016, Phys. Rev. D, 93, 043013
Macaulay E., Wehus I. K., Eriksen H. K., 2013, Phys. Rev. Lett., 111, 161301
Madau P., Dickinson M., 2014, ARA&A, 52, 415
Maldacena J., 2003, J. High Energy Phys., 2003, 013
Matarrese S., Verde L., Jimenez R., 2000, ApJ, 541, 10
McDonald P., Seljak U., 2009, J. Cosmology Astropart. Phys., 2009, 007
Nunes R. C., Vagnozzi S., 2021, MNRAS, 505, 5427
Percival W. J. et al., 2019, preprint (arXiv:1903.03158)
Qian X., Vogel P., 2015, Prog. Part. Nucl. Phys., 83, 1
Riess A. G., Casertano S., Yuan W., Macri L. M., Scolnic D., 2019, ApJ, 876, 85
Sailer N., Castorina E., Ferraro S., White M., 2021, J. Cosmology Astropart. Phys., 2021, 049
Schechter P., 1976, ApJ, 203, 297
Schlegel D., White M., Eisenstein D., 2009, in astro2010: The Astronomy and Astrophysics Decadal Survey, p. 314.
Schlegel D., Kollmeier J. A., Ferraro S., 2019, BAAS, 51, 229
Seo H.-J., Eisenstein D. J., 2007, ApJ, 665, 14
Slosar A. et al., 2019, BAAS, 51, 53
Steidel C. C., Shapley A. E., Pettini M., Adelberger K. L., Erb D. K., Reddy N. A., Hunt M. P., 2004, ApJ, 604, 534
Tegmark M., 1997, Phys. Rev. Lett., 79, 3806
Tripathi A., Sangwan A., Jassal H., 2017, J. Cosmol. Astropart. Phys., 2017, 012
Vagnozzi S., 2020, Phys. Rev. D, 102, 023518
White M., Song Y.-S., Percival W. J., 2009, MNRAS, 397, 1348
Wilson M. J., White M., 2019, J. Cosmology Astropart. Phys., 2019, 015
Yankelevich V., Porciani C., 2019, MNRAS, 483, 2078
Zhao G.-B. et al., 2016, MNRAS, 457, 2377
Zhao G.-B. et al., 2019, MNRAS, 482, 3497

[19]Except when the duration is very small.

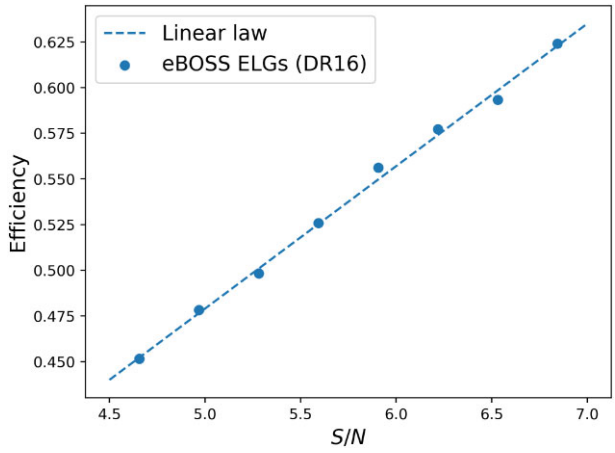

Figure A1. Efficiency as a function of the SNR for eBOSS ELGs. We also include the linear best fit.

APPENDIX A: EFFICIENCY AND SNR

In Fig. A1, we present the efficiency of the ELGs' observation for eBOSS DR16, as a function of the SNR for ELGs at $0.6 < z < 1.1$. The efficiency is the fraction of ELGs' targets (photometrically defined) that are classified as ELG spectroscopically and have a reliable redshift measurement. Its efficiency scales linearly with the SNR. We assumed that this trend would be similar for LBG at high redshift in our study.

APPENDIX B: AVERAGE EXPOSURE TIME

Given a minimal observation efficiency, some tracers need to be observed twice or three times. Since we do not consider measurements with m higher than 25 because of engineering limits, it is in practice never necessary to observe more than three times for a given tracer. We recall that $E(m)$ is the one-exposure efficiency law. The average number of observations is analytically given by

$$\frac{\langle t(m)\rangle}{t_{\rm exp}} = \begin{cases} 1 & \text{if } (C_1) \\ 1+\eta_2 & \text{if } (C_2) \\ 2-E(m)+\eta_3 & \text{if } (C_3), \end{cases} \tag{B1}$$

with the ratio,

$$\eta_2 = \frac{p_{\rm min}-E(m)}{\sqrt{2}E(m)} \text{ for } (C_2) \tag{B2}$$

$$\eta_3 = \frac{p_{\rm min}-E(m)(\sqrt{2}+1-\sqrt{2}E(m))}{\sqrt{3}E(m)} \text{ for } (C_3) \tag{B3}$$

and the conditions,

$$(C_1): E(m) \geq p_{\rm min}, \text{ only one observation is necessary} \tag{B4}$$

$$(C_2): E(m) < p_{\rm min} \text{ and } E(m)(\sqrt{2}+1-\sqrt{2}E(m)) \geq p_{\rm min} \tag{B5}$$

$$\text{two observations may be necessary} \tag{B6}$$

$$(C_3): \text{higher } m \text{ than } (C_2), \text{ three observations may be necessary.} \tag{B7}$$

Graphically, in Fig. 1

(i) ($C1$) represents the left part of the plane (full red), where only one observation is necessary;
(ii) (C_2) is the middle part, with possibly a second observation, and $\eta_2(m)$ corresponds to the vertical width of the green area; and
(iii) (C_3) is the right part with possibly three observations, and $\eta_{3t_{\rm exp}}$ is the vertical width of the blue area.

APPENDIX C: MAXIMAL MAGNITUDE DISCRETIZATION

We have

$$\frac{N_{\rm fib}\,T_{\rm sur}}{4\pi\,\eta_{\rm til}\,f_{\rm sky}} = \int_{22.5}^{m_{\rm max}} dm \int_{z_{\rm min}}^{z_{\rm min}+\Delta z} dz \underbrace{\frac{d\chi}{dz}\,\chi^2\langle t(m)\rangle\phi_{\rm LBG}(m,z)}_{f_{mz}(m,z):=}. \tag{C1}$$

We define two small steps δ_m and δ_z (typically 0.01) and transform our integrals into Riemann sums. We will thus find recursively the integer $j_{\rm max}$ such that the sum

$$S = \sum_{j=0}^{j_{\rm max}} \delta_m \sum_{i=0}^{\lfloor \Delta z/\delta_z \rfloor} \delta_z\, f_{mz}(m = 22.5 + j\delta_m, z = z_{\rm min} + i\delta_z) \tag{C2}$$

is equal to the constant on the left-hand side of equation (C1) and deduce an approximation for $m_{\rm max}$. We assume that $m_{\rm max}$ cannot be greater than 25 for practical reason since observation of fainter objects would be challenging, and because our luminosity function model does not describe LBG for higher magnitude (Wilson & White 2019). That is why we observed saturation in Fig. 2 for small volume. As the luminosity function decreases with redshift, the saturation value that corresponds to observation of every galaxy up to $m_{\rm max} = 25$ decreases with Δz.

This paper has been typeset from a TEX/LATEX file prepared by the author.